Energy Conversion and Management 237 (2021) 114129

Contents lists available at ScienceDirect

Energy Conversion and Management

journal homepage: www.elsevier.com/locate/enconman

Strongly coupled piezoelectric energy harvesters: Optimised design with over 100 mW power, high durability and robustness for self-powered condition monitoring

Yang Kuang [a], Zheng Jun Chew [a], John Dunville [b], Jim Sibson [b], Meiling Zhu [a,*]

[a] College of Engineering, Mathematics and Physical Sciences, University of Exeter, Exeter, UK
[b] Babcock International Group, UK

ARTICLE INFO

Keywords:
Piezoelectric energy harvesting
High power
Strongly coupled
Self-powered systems
Condition monitoring

ABSTRACT

Harvesting ambient vibration energy is a promising method to realise self-powered wireless sensors. However, most of the energy harvesters developed to date are not suitable for real-world applications because of low power output and/or poor durability and robustness. To overcome these challenges, this work develops a strongly coupled piezoelectric stack energy harvester (PSEH) with design considerations not just on the power output but also on the durability and robustness. The PSEH took advantages of the force amplification capability of an optimised mechanical transformer and the high coupling coefficient of a 33-mode multilayer piezoelectric stack to achieve strong coupling and therefore high-power generation. To increase the durability, the piezoelectric stack was pre-compressed to prevent the development of tensile stress, to exploit the high compressive strength of piezoelectric ceramics; the maximum dynamic stress in the mechanical transformer was kept below half of the material's fatigue limit. Plate springs were used to guide the motion of the PSEH and prevent undesired vibration to enhance robustness. A finite element model was developed for design optimisation, which links the design parameters directly to the full performance matrix including maximum power generation. When actuated at 0.5 g, 157 Hz in the lab tests, the PSEH produced a maximum average power of 140 mW with a 1-mW-bandwidth of 72 Hz and 10-mW-bandwidth of 24 Hz. The PSEH showed no performance degradation after continuously actuated at 0.3 g, 157 Hz for 7.9 h. In addition to the lab tests, on-site tests were performed by installing the PSEH in two locations of a screw air compressor. On-site tests showed that the PSEH was able to produce average power of 15.95 ± 2.3 mW and 43.19 ± 1.52 mW when the acceleration produced by the air compressor was 0.125 ± 0.012 g and 0.259 ± 0.004 g, respectively.

1. Introduction

Condition monitoring of critical or high-value assets is the most effective technique to enhance management and maintenance. It offers significant benefits of cost-saving, productivity improvement, safety and reliability to industries by providing an early indication of potential equipment failure and upgrading the conventional breakdown/preventive maintenance to predictive maintenance [1,2]. Traditionally, condition monitoring is performed with wired systems which suffer from the drawbacks of high cost and difficult installations. In these aspects, wireless sensor networks (WSNs) offer an effective solution by eliminating the cables/wires, which increases flexibility and reduces the cost of installation. However, WSNs are usually powered by conventional batteries with limited energy capacity and finite lifetime. Replacing or recharging the depleted batteries can be expensive and difficult particularly when the sensor nodes are remote or inaccessible. This challenge has been driving the worldwide research efforts in the last two decades in energy harvesting (EH) technologies, which converts ambient energy sources to electricity supplying the WSNs [3].

During the operation of machine systems, a large amount of energy exists in the form of structural vibrations, which are a good energy source to be harvested and used to power the WSNs for monitoring the working conditions. The structural vibrations can be scavenged by transduction mechanisms including piezoelectric [4], electromagnetic [5,6], electrostatic [7] and triboelectric [8] through the inertial of a proof mass, all of which have been comprehensively investigated and

* Corresponding author.
E-mail address: m.zhu@exeter.ac.uk (M. Zhu).

https://doi.org/10.1016/j.enconman.2021.114129
Received 3 December 2020; Accepted 1 April 2021
Available online 17 April 2021

are capable of providing a useful amount of energy. Among these transduction mechanisms, piezoelectric energy harvesters (PEHs) have gained the most attention due to their high energy density, scalability and simple structures [9]. So far, innumerable PEHs have been developed with power output widely varying from microwatts to tens of milliwatts [10]. Although some of them have demonstrated their ability to power wireless sensor nodes in the lab, the real-world applications are still very rare, mainly due to insufficient power output for the required tasks and/or poor durability and robustness.

The majority of PEHs work in a bending mode with configurations such as cantilever [11] or the doubly-clamped beam [12]. They have the advantages of low stiffness, low resonance frequency, simple structure and easy for MEMS fabrication. The power output of bending-mode PEHs reported in the literature mostly varies from a few microwatts to a few milliwatts [10], largely depending on the size of the PEH and the actuating amplitude, though some prototypes with high power generation have been reported recently. He *et al.* [13] recorded an average power of 15.4 mW from a piezoelectric cantilever actuated by a rotational motion at 150 revolutions per minutes. Kim *et al.* [14] developed a piezoelectric cantilever with an array of four piezoelectric layers ($35 \times 37 \times 0.16$ mm^3 each) and recorded nearly 30 mW of power when an acceleration of 1 g at 120 Hz was applied. Jeon *et al.* [15] developed a displacement amplification mechanism and a deformation guide to increase the power output of a cantilever for road displacement energy harvesting. The piezoelectric layer with peak stress over 150 MPa produced an instantaneous of 60.3 mW. The main concern of bending-mode PEHs is the stress concentration in the piezoelectric layer, which would significantly reduce the durability of the piezoelectric material and constrain the power output. Piezoelectric ceramics are born with internal and surface cracks, which propagate progressively under tension. As a result, piezoelectric ceramics have a low tensile (~45 MPa) and bending (~80 MPa) strength [16,17]. The fatigue limits of piezoelectric ceramics working under dynamic stress are even lower (27.6–48.3 MPa for bending [16]). Okayasu *et al.* [18] showed that fatigue life for commercial bulk PZT under bending stress of 60 MPa is 10^5 cycles. Kim et al [19] observed line cracks on a piezoelectric bimorph cantilever after 2–3 min of operation.

To improve the power output, longitudinal-mode PEHs have been researched, which usually employ a mechanical transformer to amplify the longitudinal stress in piezoelectric plates/stacks. The longitudinal-mode PEHs were initially developed to harvest energy directly from compressive forces and work at a non-resonant state [19]. They have been intensively investigated for applications such as footfall [20,21], road surfaces [22,23], floor tile [24] and pressure ripples of hydraulic pipelines [25]. The use of longitudinal-mode PEHs for inertial and resonant energy harvesting is relatively limited, perhaps due to the concerns of the high resonance frequency. Xu et al. [26] combined cymbal structures with cantilever beams to lower the resonance frequency and increase the power generation from low-frequency vibration. The fabricated prototype produced a power of 3.7 mW under an acceleration of 3.2 g at 102 Hz. Later, Yang et al. [27] proposed a nonlinear energy harvester with a multi-stage force amplifier, which included a bridge-type force amplifier and elastic beams. The use of the multi-stage structure increased the power output and reduced the resonance frequency to 26 Hz, at which 54.7 mW was produced with an acceleration of 0.5 g [28]. Wang *et al.* [29] developed a PEH with a two-stage force amplifier and three multilayer piezoelectric stacks. With a proof mass of 0.1 kg and acceleration of 0.1 g, the PEH produced a power density as high as 2642 mW/g^2 at 37 Hz. Although the longitudinal-mode PEHs showed promising power output with reduced or eliminated stress concentration, care still must be taken on its durability as the piezoelectric material has a low tensile strength. Zhao *et al.* [30] found a piezoelectric plate with a bridge-type force amplifier failed when the peak stress exceeded ~ 30 MPa.

Depending on the electromechanical coupling coefficient figure of merit K^2Q_M (K being the electrotechnical coupling coefficient and Q_M the mechanical quality factor), PEHs can be generally grouped into weakly coupled ($K^2Q_M < 2$) and strongly coupled ($K^2Q_M > 2$) [31]. Strongly coupled PEHs have two identical power peaks in the resonance region compared to the single power peak of weakly coupled PEHs and therefore can increase the power output and bandwidth. The strong coupling has been mainly observed in bending-mode piezoelectric cantilevers with power output from a few to hundreds of microwatts [31–33]. In the previous work [34], the present authors for the first time discovered strong coupling behaviours on a longitudinal-mode piezoelectric stack energy harvester (PSEH) and developed a finite element model to investigate the mechanism of strong coupling. The PSEH produced 5.2 mW when actuated by an acceleration of 0.25 g. In this work, the PSEH is further designed and optimised to exploit the advantages of both strong coupling and longitudinal-mode for real-world applications. Unlike most previous studies with little consideration on the durability and robustness, this work has not only been devoted to increasing the power output and bandwidth but also simultaneously to upholding the durability and robustness so that the developed PSEH fully meets the requirement of real-world applications. Finite element modelling is performed to optimise the power output of the PSEH while keeping the stress below half of the material's fatigue limit. Novel strategies have been implemented to ensure durability and robustness in the harsh industrial environment. The design, optimisation, lab testing and on-site testing of the PSEH are presented in this paper. While maintaining a safety factor (SF) machine larger than two, the fabricated PSEH produces a power output of 140 mW, which is 2.5 times the state-of-the-art inertial PEHs. During on-site testing, the PSEH produces average power of 15.95 ± 2.3 mW and 43.19 ± 1.52 mW when actuated by an acceleration of 0.125 ± 0.012 g and 0.259 ± 0.004 g, respectively.

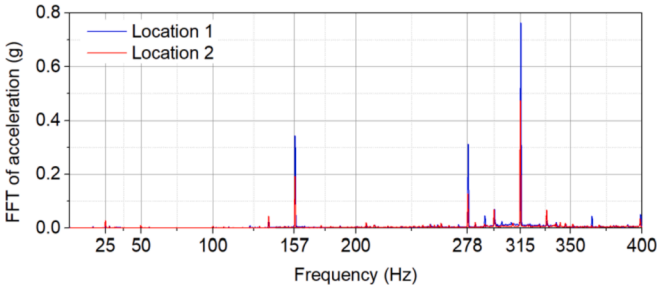

Fig. 1. Frequency spectrum of the acceleration measured on a screw compressor.

2. Design of the energy harvester

2.1. Design targets

This work takes screw compressors (G-Drive, ALMiG Compressor GmbH) installed in Babcock International Group (Plymouth, UK) as a study case to develop a durable and robust PEH for a self-powered machine monitoring system. To determine the working frequency of the PEH, the vibration of one screw compressor was measured by an accelerometer (8786A5, Kistler). The frequency spectrum of the acceleration measured at two potential installing locations near the bearings is presented in Fig. 1. The acceleration components at 25 Hz correspond to the rotational speed of the motor (RPM of 1500). The main vibration components are located at 157, 278 and 315 Hz. Higher orders of harmonic vibration components were observed but not presented herein because of their low values.

The electric power output of a single-degree-of-freedom energy harvester working at resonance can be expressed as [35,36]

$$P = \frac{m\xi_e A_0^2}{4\omega_0 \xi_T^2} = \frac{k\xi_e A_0^2}{4\omega_0^3 \xi_T^2} \quad (1)$$

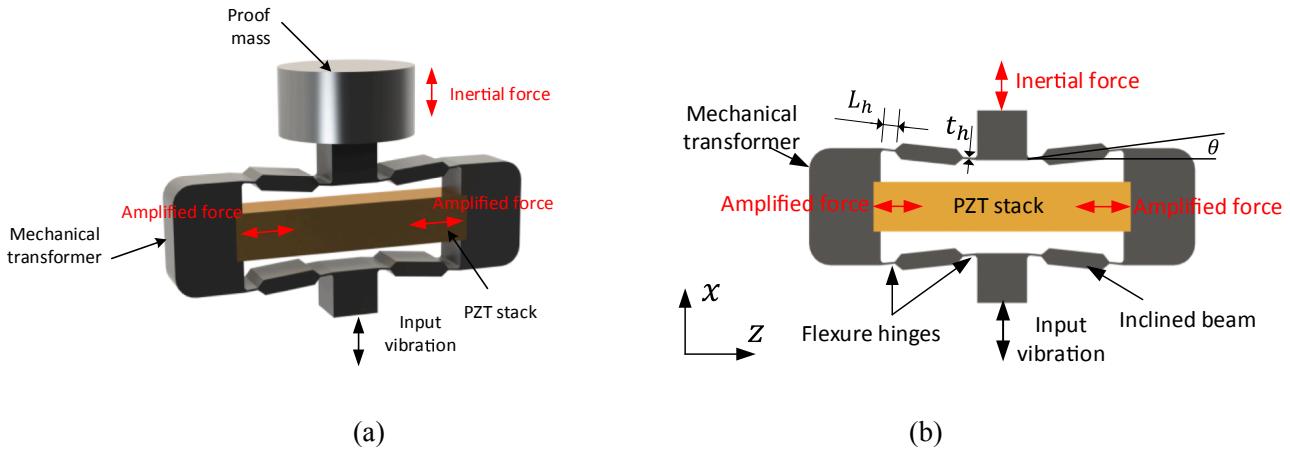

Fig. 2. Schematics of the strongly coupled piezoelectric stack energy harvester: (a) perspective view and (b) 2D view with the proof mass hidden.

where m is the mass; k the stiffness; ξ_e the electrical damping due to energy harvesting; ξ_T the total damping including both mechanical and electrical damping; A_0 the excitation acceleration amplitude; $\omega_0 = \sqrt{k/m}$ the resonance frequency. Eq. (1) suggests that for a specific EH with a constant stiffness $k$and damping factors, the power output is proportional to A_0^2/ω_0^3. According to the measured vibration spectrum, the value of A_0^2/ω_0^3 at 157 Hz is the highest among the three main vibration components. Therefore, the PEH is designed to resonant at around 157 Hz.

Although the measured vibration amplitude at 157 Hz is $<$0.35 g, the maximum input acceleration for the designed EH is set to be 0.5 g and a safety factor (SF) of 2 is applied to ensure durability and robustness even when the vibration frequency and amplitude are varied due to the variation of the compressor's loading conditions.

2.2. Working mechanism of the strongly coupled PSEH

The EH designed in this study is a piezoelectric stack energy harvester (PSEH), which has been proved to be strongly coupled and exhibit two identical power peaks across the resonance region. Fig. 2 shows the schematic of the PESEH. It consists of a PZT stack polarised along the z-axis, a mechanical transformer and a proof mass. The mechanical transformer has four inclined beams with an inclined angle of $\theta < 45^\circ$. The inclined beams are designed to be thin on the ends and thick in the middle. The thin ends serve as flexure hinges to allow the easy bending of the beams while the thick middle parts reduce the deformation of the beams to minimise the storage of elastic energy. Such a transformer has been proved to have the ability to amplify the input force and reduce the structural stiffness [34]. As a vibration along the x-axis is applied to the PSEH, an inertial force is exerted to the mechanical transformer due to the proof mass. The mechanical transformer amplifies and redirects the input to the z-axis force applied on the PZT stack to produce electricity.

Compared to the traditional bending-mode energy harvesters, the PSEH offers four advantages for vibration energy harvesting. First of all, the piezoelectric material operates at the 33-mode in the PSEH, as opposed to the 31-mode in bending-mode PEHs. Since piezoelectric materials have a higher electromechanical coupling coefficient Kin a 33-mode than in a 31-mode, the use of 33-mode leads to a higher value of coupling efficiency figure of merit K^2Q_M, which is critical in achieving strongly coupled PEH. Moreover, higher K means a higher efficiency of converting mechanical energy to electricity. Secondly, the stress is evenly distributed on the piezoelectric material, in contrast to the severe stress concentration in bending-mode PEHs. The even distribution of the stress allows the piezoelectric material to generate higher electric power with lower peak stress. Thirdly, the mechanical transformer can amplify the input inertial force and thus increase the power generation, which has been widely exploited for energy harvesting from low-frequency compressive forces [37,38]. The last but not least, the mechanical transformer reduces the stiffness and thus the resonance frequency of the PSEH. The PZT stack operates in its longitudinal mode in the PSEH [34]. Because of its high stiffness, the PZT stack in the longitudinal mode has a resonance frequency in the range of tens of kilohertz, which is far higher than the frequency of ambient vibrations. The reduction of the stiffness and resonance frequency by the mechanical transformer makes it possible to match the resonance frequency of PSEH to the ambient vibration and thus to maximise the energy generation.

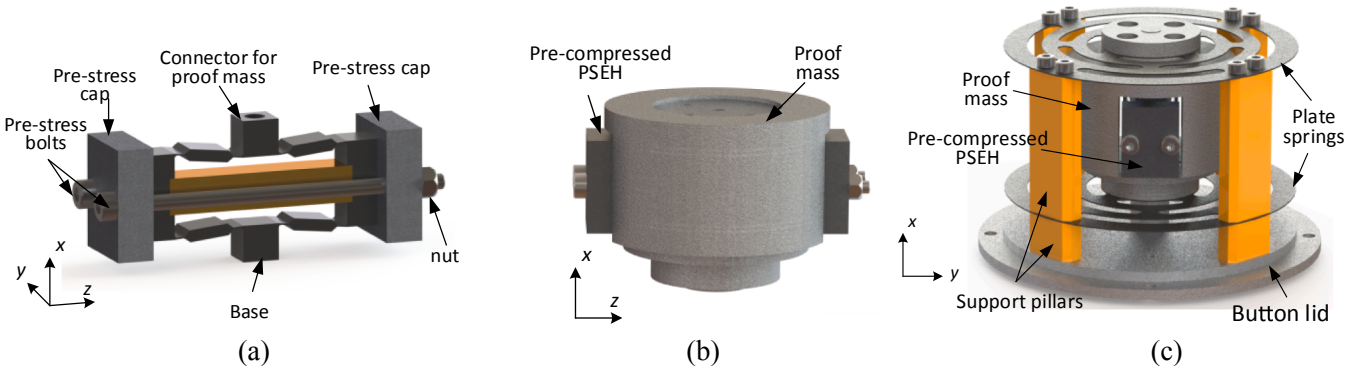

Fig. 3. Design considerations to increase the durability and robustness of the PSEH: (a) an auxiliary rig is designed to apply pre-compressive stress in the PZT stack; (b) the proof mass is designed with a lowered centre; (c) two plate springs are designed to minimise motions in undesired directions.

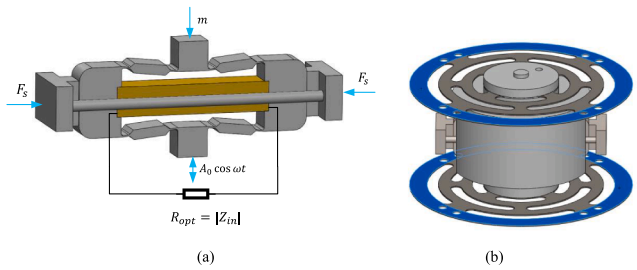

Fig. 4. Schematics of the finite element models: (a) FEM without plate springs used for the parametric design stage (b) full model of the PSEH.

2.3. Durability and robustness considerations

The PZT stack in the strongly coupled PSEH experiences both tensile and compressive stress during operation. Because of the propagation of internal flaws in tension, piezoelectric ceramics have low tensile strength. The tensile stress in the PZT stack severely reduces the lifetime of the PSEH. However, the propagation of the internal flaws is constrained when the piezoelectric ceramics are in compression, leading to high compressive strength (>600 MPa). As a result, pre-compressing piezoelectric ceramics to prevent the development of tensile stress is a common procedure to increase the durability of piezoelectric actuators [39]. Pre-compressed piezoelectric actuators have shown lifetime > 10^{10} cycles with little degradation [40,41]. To exploit the high strength and durability of piezoelectric ceramics in a compressive mode, an auxiliary rig was designed to apply static compressive stress to the PZT stack, as shown in Fig. 3 (a). The PSEH is placed between two pre-stress caps, which are fastened by two bolts. Once the nuts are tightened, the caps compress the PSEH and apply static compressive stress in the PZT stack.

The PSEH is designed to oscillate along the *x*-axis. However, ambient vibrations are usually multi-directional, leading to multi-directional forces applied to the mechanical transformer. The forces applied in undesired directions cause a moment to the mechanical transformer, which can be harmful. To reduce this moment, the proof mass was designed to enclose the mechanical transformer to lower the mass centre, as shown in Fig. 3 (b). To further improve the stability and robustness, the proof mass was connected to two plate springs, one on each end, as shown in Fig. 3 (c). The outer rings of the plate springs are coupled to the base (Fig. 3 (a)) of the mechanical transformer through the support pillars and the bottom lid. The plate springs make sure that the proof mass is free to move along the *x*-aixs while its motions in other directions are constrained. Moreover, with the two springs, the PSEH can be installed at any angle relative to gravity.

3. Modelling and design optimisation

3.1. Finite element modelling methods

Finite element models were developed in COMSOL Multiphysics® to optimise the design and predict the performance of the PSEH. Most of the previous finite element models of longitudinal-mode PEHs can only optimise the performance in terms of intermediate values such as force amplification factor and energy transmission efficiency [29,38,42]. The FEM developed in this work is a piezoelectric-circuit coupled model, which directly links the design parameters to the electric power output, enabling optimisation in terms of the final output of the PSEH. Moreover, the FEM in this study adopted the method developed in the previous study for strongly coupled PEHs [34], which first analyses the internal impedance of the PEH and then uses the impedance magnitude as the optimal load resistance for power generation.

In the design optimisation stage where the effects of key design parameters were investigated, the FEM did not include the plate springs, as shown in Fig. 4 (a), to reduce the scale of the model and save the computation time. The bolts with threads and nuts were simplified as two rods, the diameter of which is the pitch diameter of the threads. A pair of static compressive forces F_s was applied on the caps to introduce the pre-stress. The proof mass *m*was included in the model by a boundary condition in COMSOL without building a physical mass. A harmonic acceleration $A_0 \cos \omega t$ was applied to the base of the mechanical transformer. The amplitude of the acceleration $A_0$was set to 0.5 g unless specified. The PZT stack was modelled as a single layer piezoelectric ceramic with dimensions of 7 × 7 × 36 mm^3, although a multi-layered stack would be used in the experiment. While the total volume of the PZT stack is constant, the number of layers affects the internal impedance magnitude, the voltage and current generated but it does not affect the power output. The rest of the PSEH was modelled as spring steel. The material properties are listed in Table 1. The material properties of piezoelectric material PIC252 were provided by the material supplier (PI ceramic GmbH). The mechanical damping was specified as the mechanical quality factor Q_M, which was estimated to be 100. The material properties are assumed not to change with the acceleration amplitude.

Table 1
The material properties of the piezoelectric material (PIC 252) and spring steel.

Parameters	Values
Piezoelectric stack	
Density (kg/m^3)	7800
s_{11}^E(×10^{-12} m^2/N)	16.06
s_{12}^E(×10^{-12} m^2/N)	−5.68
s_{13}^E(×10^{-12} m^2/N)	−7.45
s_{33}^E(×10^{-12} m^2/N)	27.0
s_{44}^E(×10^{-12} m^2/N)	46.99
s_{66}^E(×10^{-12} m^2/N)	43.50
d_{31}(×10^{-12} m/V)	−186.7
d_{33}(×10^{-12} m/V)	399.6
d_{15}(×10^{-12} m/V)	617.4
$\varepsilon_{11}^T/\varepsilon_0$	1850
$\varepsilon_{33}^T/\varepsilon_0$	1750
Spring steel	
Density (kg/m^3)	7850
Young's modulus (GPa)	207
Poisson's ratio	0.3

The electrodes of the PZT stack were connected to the optimal load resistance R_{opt}, which yields the maximum power generation. Before simulating the power output, the internal impedance Z_{in} of the PSEH was analysed by computing the performance of the PSEH in an actuator mode: a voltage was applied to the PZT stack to compute the current generated to calculate the internal impedance Z_{in} [34]. The magnitude$|Z_{in}|$ of the internal impedance is the optimal load resistance [31,43] and was assigned toR_{opt}.

Following the determination of the optimal design, a full model of the PSEH (Fig. 4 (b)) was built. Compared to the model in Fig. 4 (a), the full model included the two plate springs and the physical proof mass. The support pillars and the bottom lid were not built. Their clamping effect was modelled by coupling the outer rings of the plate springs (highlighted in blue) to the input base of the mechanical transformer in terms of displacement. Other boundary conditions of the full model are the same as the model in Fig. 4 (a).

3.2. Design optimisation

In this section, the model without plate springs was used to study the effects of key design parameters on the performance of the PSEH. These parameters include the size of bolts, inclined angle θ, hinge length L_h and hinge thickness t_h, which are shown in Fig. 2 (b). The objective of the

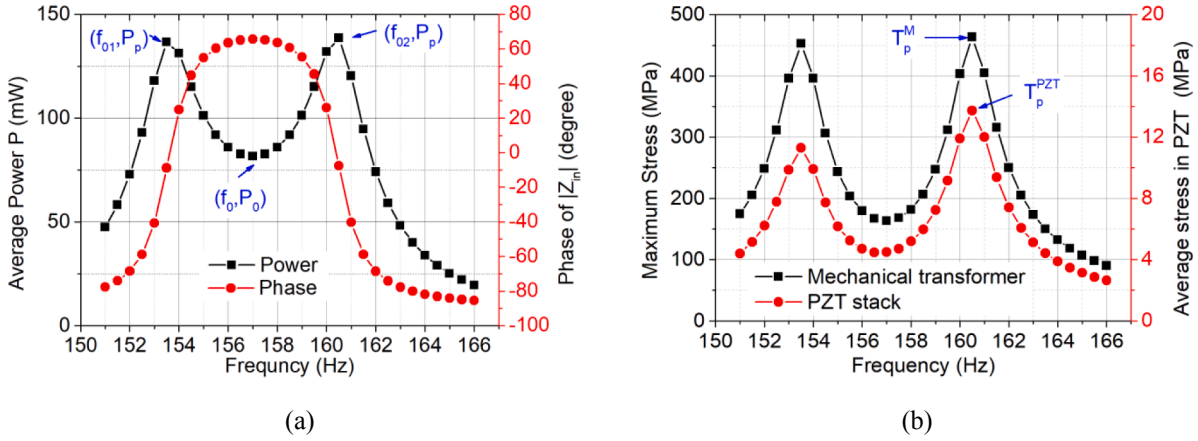

Fig. 5. Representative performance of the PSEH: (a) average power and the phase of the internal impedanceZ_{in}; (b) the peak von Mises stress in the mechanical transformer and the average von Mises stress in the PZT stack.

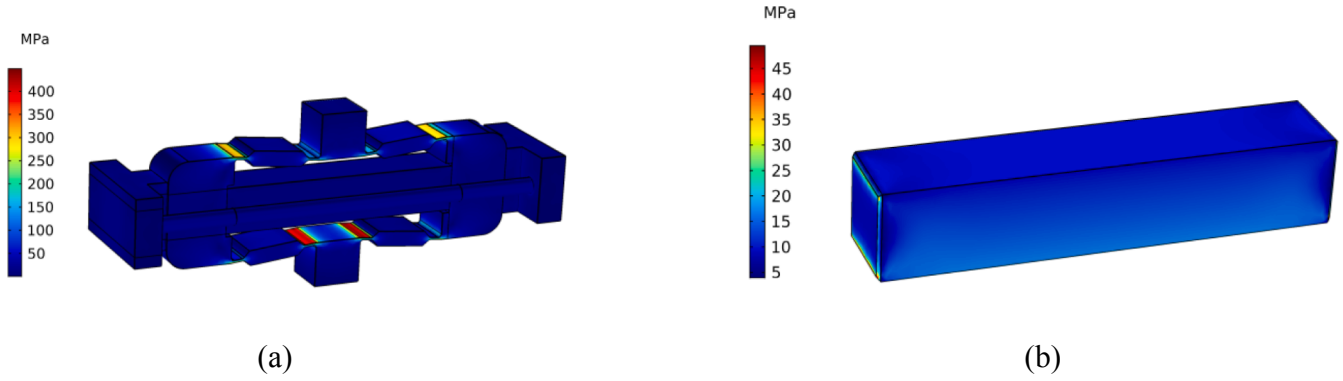

Fig. 6. Von Mises stress distribution in (a) the PSEH and (b) the PZT stack when the PSEH is actuated at 0.5 g, 159.5 Hz.

design optimisation is to increase the power output and bandwidth while maintaining sufficient durability.

(i) Representative performance of the PSEH

The representative output performance of the PSEH are presented in Fig. 5, which was obtained with pre-stress bolts of M3, θ=6°, t_h=0.3 mm and L_h = 2 mm. The electric power shows two identical peaks P_p at f_{01} and f_{02}, and a local minimum P_0 at f_0.It is noted that the power at each frequency was obtained with the PSEH connected to the optimal load resistance and therefore these power values are the maximum power at the corresponding frequencies. The dual-peaks in power output are a signature of strongly-coupled PEHs. They are located at frequencies where the phase of the internal impedance $|Z_{in}|$ is zero, i.e. the internal impedance is purely resistive, as can be observed in Fig. 5 (a). At zero-phase frequencies, conjugate matching of the internal impedance can be achieved by the load resistance, leading to the maximum power transfer and peak power output [31,34]. The strong coupling of the PSEH is attributed to the large electromechanical coupling coefficient of $K$and mechanical quality Q_M of the PSEH, leading to the electromechanical coupling figure of merit$K^2Q_M > 2$, which is the prerequisite for strong coupling. The value of K can be calculated by [32]

$$K^2 = \frac{f_{02}^2 - f_{01}^2}{f_{01}^2} \quad (2)$$

The value of K^2 calculated from the results in Fig. 5 (a) is 0.093. WithQ_M = 100, K^2Q_M is 9.3, which also implies the PSEH is strongly coupled.

The stress in the mechanical transformer and the PZT stack exhibits similar trends as the power output, as shown in Fig. 5 (b). The locations of the stress peaks across the resonance region coincide with the power peaks. The stress of the mechanical transformer presented in Fig. 5 (b) is the maximum von Mises stress at each frequency, which is always located at the flexure hinges because of the large bending motion and the stress concentration, as shown in Fig. 6 (a). In the PZT stack, the stress is distributed almost uniformly, although high stress is observed

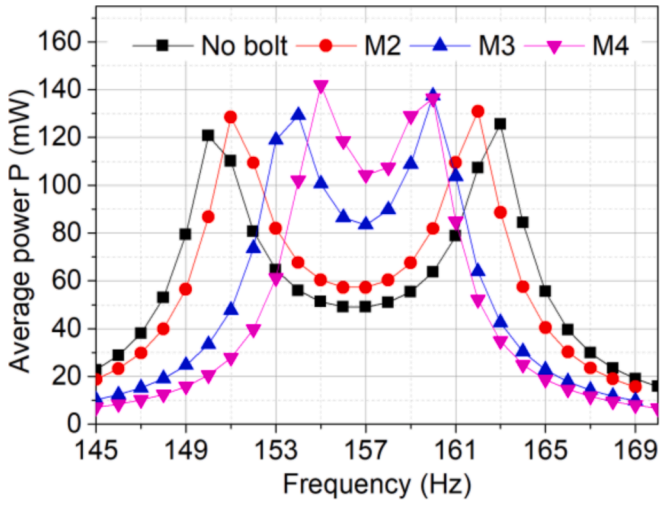

Fig. 7. Effects of the size of the pre-stress bolts on the average power output spectrum of the PSEH.

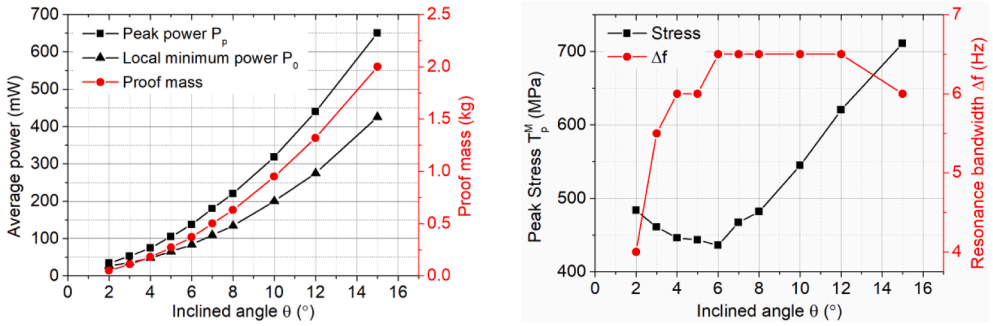

Fig. 8. The effects of the inclined angle θ on: (a) the power outputs and proof mass; (b) the maximum von Mises stress in the mechanical transformer and the resonance bandwidth Δf when$t_h = 0.3$ mm and$L_h = 2$ mm.

on the surfaces where the PZT stack interfaces the mechanical transformer, as shown in Fig. 6 (b). For the PZT stack, the volume-average von Mises stress is considered and presented in Fig. 5 (b). The stress peaks in the mechanical transformer and PZT stack are denoted as T_p^M and T_p^{PZT}, which will be used to evaluate the strength and durability of the PSEH.

Although the PSEH shows power peaks at f_{01} and f_{02}, the PSEH will be designed with f_0 matching the ambient vibration frequency (157 Hz) so that it can have the maximum tolerance for the shift of actuating frequency. The mechanical transformer in this study will be made of spring steel 60Si2CrVA. With proper heat treatment and surface finish, the fatigue limit of spring steel 60Si2CrVA is about ~ 750 MPa [44]. To uphold the lifetime of the mechanical transformer, the peak stress T_p^M should be lower than the fatigue limit of the material. In this study, T_p^Min the mechanical transformer would be kept less than 375 MPa to achieve a safety factor of 2 and ensure the longevity of the mechanical transformer.

(ii) Effects of the pre-stress bolts

The power outputs of the PSEH with M2, M3 and M4 pre-stress bolts are compared with that of the PSEH without pre-stress bolts in Fig. 7. The proof mass was varied to make sure$f_0 = 157$ Hz. The proof mass for no bolt, M2, M3 and M4 bolts are 0.338, 0.350, 0.370 and 0.385 kg, respectively. As the bolt size increases, the power peak $P_p$increases slightly due to the increased proof mass. The more remarkably variation is the reduction of $\Delta f = f_{02} - f_{01}$ as the bolt size increases. Δf is the bandwidth between the two zero-phase resonance frequencies and is therefore referred to as resonance bandwidth in this study. The resonance bandwidth reflects the electromechanical coupling coefficient of the PSEH, the square of which is the ratio of the stored electrical energy to the input mechanical energy and can be calculated by Eq. (2). The calculated values of K^2 for no bolt, M2, M3 and M4 bolts are 0.18, 0.15, 0.079 and 0.066, respectively. As the bolt size increases, a larger portion of the input mechanical energy is absorbed by the bolts, leading to a reduced portion of input mechanical energy to the piezoelectric material. As a result, the ratio of the converted electrical energy to the total input mechanical energy is reduced, i.e. the electromechanical coupling coefficient of the PSEH is reduced. Although K^2 is reduced by the pre-stress bolt, the value K^2Q_M is always >2. K^2Q_M for no bolt, M2, M3 and M4 bolts are 18.1, 15.1, 7.9 and 6.6, respectively. While the bolt size has little effect on the peak power output, a smaller bolt is preferred for the broader resonance bandwidth Δf. However, the bolt size has to be large enough to withstand the dynamic stress on the threads. In this work, considering the strength of the threads, M3 was selected as the size of the pre-stress bolts.

(iii) Effects of the geometry of the mechanical transformer

After the bolt size had been determined, simulations were performed to study the effects of geometrical parameters of the mechanical transformer including the inclined angle θ, the hinge thickness t_h and the hinge length L_h, which are denoted in Fig. 2 (b). For each configuration, the proof mass was varied to ensure $f_0 = 157$ Hz. The power output of the PSEH with M3 bolts is as high as 130 mW as shown in Fig. 7. This power is even sufficient to continuously supply high-power-consumption sensors such as acoustic emission sensors [45], which are commonly used in condition monitoring and consume tens of milliwatts. The design objective of the mechanical transformer's geometry is therefore mainly focused on maximising the resonance bandwidth while keeping the maximum stress below half of the fatigue limit.

The effects of the inclined angle θ on the performance of the PSEH with $t_h = 0.3$ mm and$L_h = 2$ mm are presented in Fig. 8. As θincreases, the proof mass required to maintain $f_0 = 157$ Hz is increased, as shown in Fig. 8 (a). This suggests that the stiffness of the mechanical transformer increases with θ. Due to the increase of the proof mass, both the power peak $P_p$and the local minimum power P_0go up with θ. Δf has its

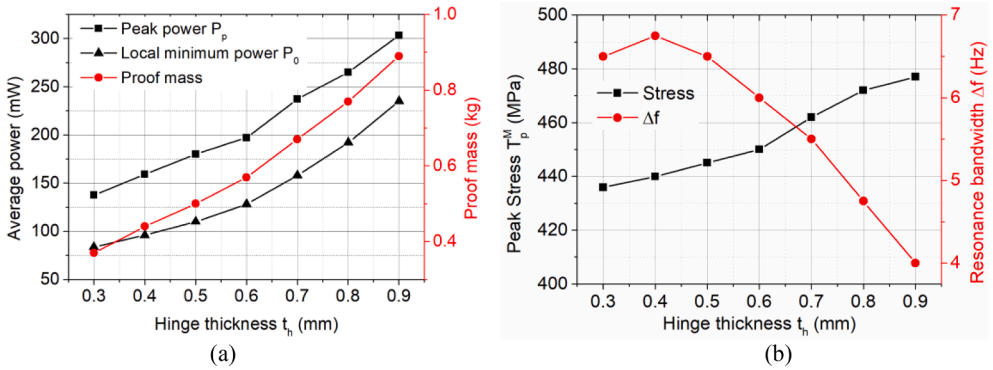

Fig. 9. The effects of hinge thickness t_h on: (a) the power outputs and proof mass; (b) the maximum von Mises stress in the mechanical transformer and the resonance bandwidth Δf when$\theta = 6°$ and$L_h = 2$ mm.

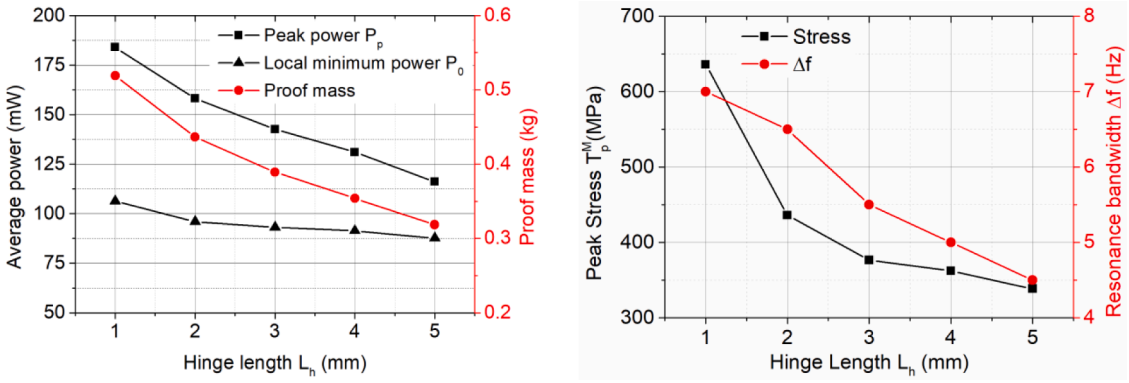

Fig. 10. The effects of hinge length L_h on: (a) the power outputs and proof mass; (b) the maximum von Mises stress in the mechanical transformer and the resonance bandwidth Δf when$\theta = 6^\circ$ and$t_h = 0.4$ mm.

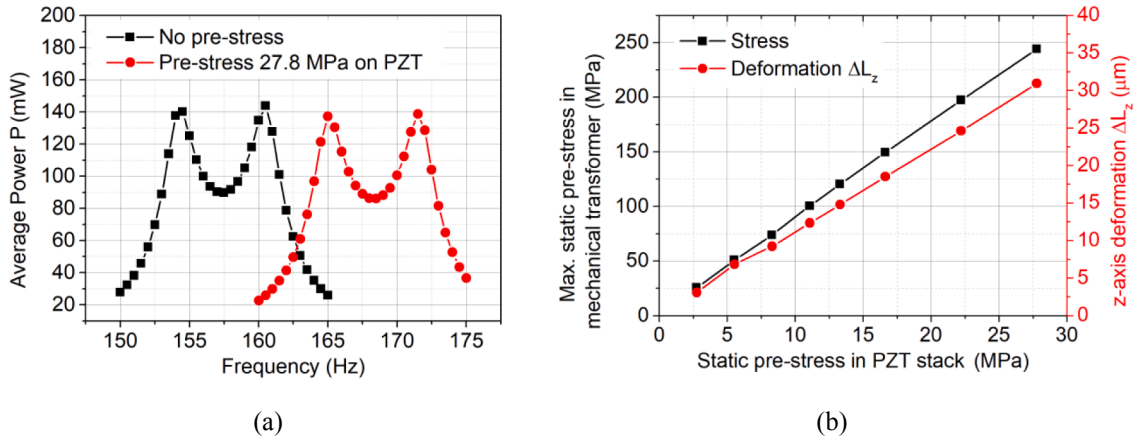

Fig. 11. Performance of the PSEH at different static pre-stress in the PZT stack: (a) average power at different frequencies and (b) the maximum static von Mises stress in the mechanical transformer and the deformation ΔL_z of the mechanical transformer along the z-axis.

maximum value of 6.5 Hz when θ is between 6° and 12°, as shown in Fig. 8 (b). The peak stress in the mechanical transformer has the minimum value of 435 MPa when$\theta = 6^\circ$. Further increasing θ produces higher power but at the cost of higher peak stress in the mechanical transformer. The inclined angle θ selected for the PSEH is 6°.

Fig. 9 shows the effects of the hinge thickness t_h on the performance of the PSEH with$\theta = 6^\circ$ and$L_h = 2$ mm. As the hinge becomes thicker, it becomes more difficult to flexure. As a consequence, the stiffness of the PSEH is increased and a larger proof mass is required to maintain the resonance frequency (Fig. 9 (a)). The increase of the proof mass is accompanied by the increase of power generation. The larger thickness also leads to higher stress in the mechanical transformer, as shown in Fig. 9 (b). The maximum value of Δf is observed when$t_h = 0.4$ mm. This value was therefore selected for the PSEH.

Fig. 10 shows the effects of the hinge length L_h on the performance of the PSEH with$\theta = 6^\circ$ and$t_h = 0.4$ mm. As L_h increases, the hinges become more flexible, resulting in the reduction of the stiffness. Therefore, to maintain the resonance frequency, the proof mass required is reduced, giving rise to the decrease in the power output. Moreover, as L_h increases, the deformation of the inclined beams increases. As a result, more energy is stored in the inclined beams, leading to the reduction of the electromechanical coupling coefficient and Δf of the PSEH (Fig. 10 (b)). The more compliant hinges suffer less stress concentration and therefore has lower peak stress. To make sure the peak stress in the mechanical transformer is less than 375 MPa, L_h was selected as 3 mm where$T_p^M = 370.8$ MPa.

3.3. Effects of the static compressive pre-stress

Based on the above studies, the geometrical parameters of the mechanical transformer are selected as$\theta = 6^\circ$, t_h=0.4 mm and$L_h = 3$ mm. The electric power output of the optimised PSEH with a proof mass of 0.39 kg and without pre-stress is presented in Fig. 11 (a). The power peaks P_p are 143.8 mW at 154.5 and 160.5 Hz, leading to$\Delta f = 6$ Hz. The local minimum power P_0 is 89.6 mW at 157.5 Hz. The amplitude of the dynamic von Mises stress T_p^{PZT}in the PZT stack was found to be 13.9 MPa at 160.5 Hz. Static pre-compressive stress of 27.8 MPa was decided to apply onto the PZT stack to ensure a safety factor of 2. Fig. 11 (a) shows the power output of the PSEH when a pre-stress of 27.8 MPa was introduced on the PZT stack by applying a static compressive force F_s (Fig. 4 (a)). The resonance frequency is increased by the pre-stress because the inclined angle θ is increasd by the pre-stress.

In addition to pre-stressing the PZT stack, the static compressive force introduces static stress in the mechanical transformer. Fig. 11 (b) shows that the maximum static von Mises stress and the z-axis deformation ΔL_z of the mechanical transformer increase linearly with the static pre-stress in the PZT stack. When the static stress in the PZT stack is 27.8 MPa, the mechanical transformer is deformed by 30.2 μm along the z-axis and has maximum stress of nearly 250 MPa. Because the static stress is tensile in some areas of the hinges, it reduces the fatigue limit of the mechanical transformer [46]. To apply the required static compressive stress in the PZT stack but avoid the high level of static

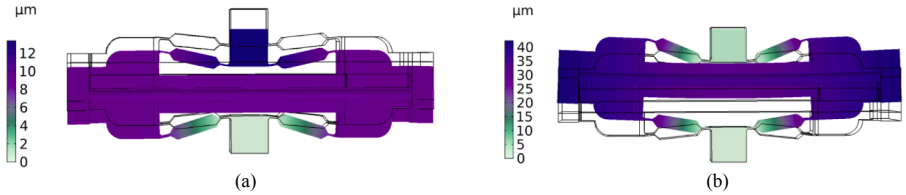

Fig. 12. (a) The designed vibration mode of the PSEH at around 157 Hz and (b) identified harmful vibration mode. The original shape is shown in the wireframe while the deformed shape is shown in colour contour. The colour contour represents the normalised displacement in μm.

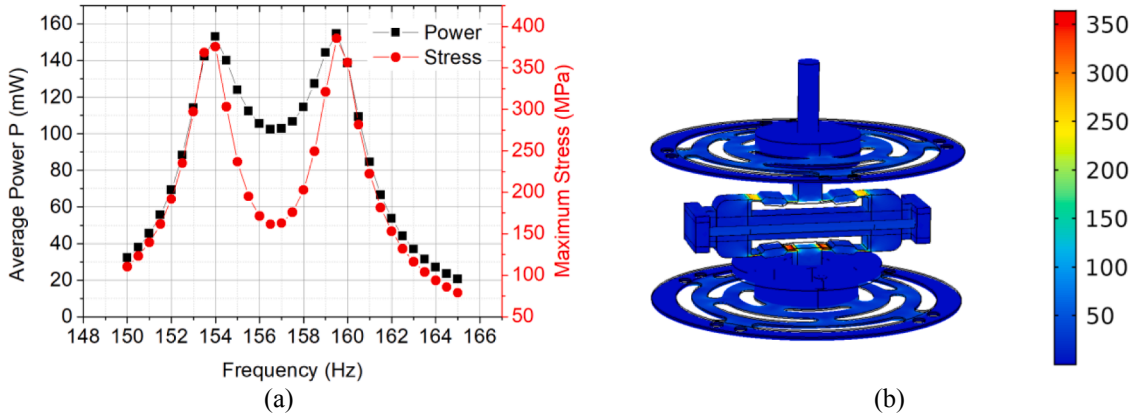

Fig. 13. Performance of the PSEH with two plate springs: (a) power outputs and the maximum von Mises stress in the mechanical transformer and (b) the von Mises stress at 159.5 Hz (unit: MPa; the proof mass is hidden to view the stress in the mechanical transformer).

stress in the mechanical transformer, the PZT stack and the mechanical transformer were designed to be assembled with an interference fit, which will be detailed in the fabrication section.

3.4. Modal shape studies

Most ambient vibrations have multiply frequency components, as in the case of the compressor in this study. On the other hand, although an EH is usually designed to work at a specific vibration mode, multiple vibration modes exist and some of them, when excited to resonate, can damage the EH. Therefore, avoiding the resonance of harmful vibration modes is necessary to ensure the robust operation of an EH.

For the PSEH, the designed vibration mode at around 157 Hz is shown in Fig. 12 (a), where the maximum displacement is located at the top connector to the proof mass. The identified harmful vibration model is shown in Fig. 12 (b), where both the top connector and the base of the mechanical transform are stationary. This mode once actuated at high amplitude, causes large bending motion and excessive stress in the hinges, leading to the failure of the mechanical transformer. For the optimised PSEH, the resonance frequency of this vibration mode is 380 Hz, which is away from the large vibration component at 314 Hz. Therefore, the resonance of the harmful vibration mode will not be excited.

3.5. The optimised design with plate springs

With the parameters of the mechanical transformer determined, two plate springs with a thickness of 0.4 mm were assembled to the PSEH along with the specially designed proof mass. Since the plate springs increased the stiffness of the PSEH, the proof mass was increased to 0.41 kg to maintain the resonance frequency. The PSEH with the plate springs produces power peaks of 154 mW at 154 Hz and 159.5 Hz (Fig. 13 (a)). The local minimum power is 102.4 mW at 157 Hz. The peak stress in the mechanical transformer is recorded as 385.5 MPa at 159.5 Hz, which is located at the hinges (Fig. 13 (b)). The peak stress is slightly higher than the target of 375 MPa. However, as will be shown in Section 4.2, the simulation slightly underestimated the mechanical damping at high vibration levels. With an increase in the mechanical damping to match the

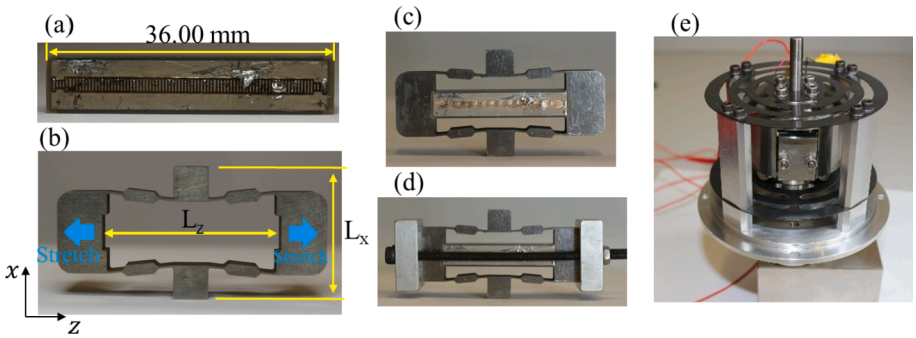

Fig. 14. Fabrication of the PSEH: (a) the PZT stack: (b) the mechanical transformer manufactured by electrical discharge machining; (c) the PZT stack and the mechanical transformer assembled with an 'interference fit'; (d) pre-stressing caps and bolts were installed and tightened; (e) the PSEH with the proof mass and plate springs installed.

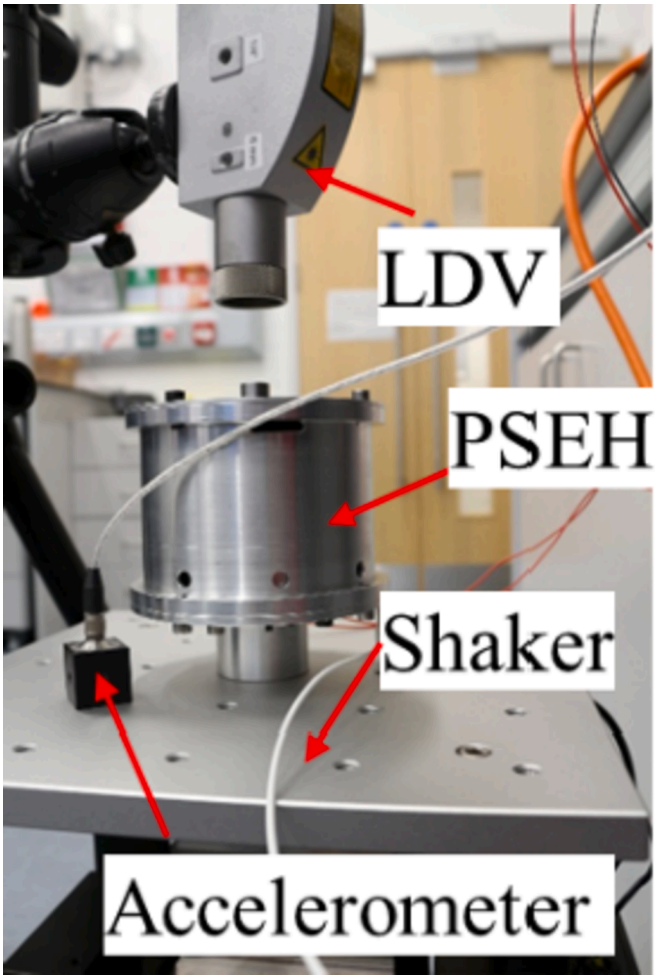

Fig. 15. Experimental setup for the lab tests.

experiment, the peak stress simulated is 330 MPa, which leaves a safety factor > 2 as the fatigue limit is ~ 750 MPa. The low stress relative to the fatigue limit ensures the lifetime and durability of the PSEH. Δf, 5.5 Hz is slightly reduced compared with the configuration with the same mechanical transformer but without the plate springs. This is because the plate springs stores elastic energy and reduces the electromechanical coupling factor of the PSEH, similar to the effects of the pre-stress bolts.

4. Fabrication and lab tests

4.1. Fabrication

The PZT stack used for the PSEH is a multilayer piezoelectric actuator (PICMA® P-887.91, PI ceramic) with dimensions of 7 × 7 × 36 mm^3, as shown in Fig. 14 (a). The PZT stack consists of ~560 layers of active piezoelectric ceramic operating in 33-mode (PIC252, layer thickness: ~60 μm including electrodes), and two passive piezoelectric layers (~0.5 mm thick), one on each end. The active piezoelectric ceramic layers are electrically connected in parallel. The mechanical transformer was manufactured by electrical discharge machining out of spring steel 60Si2CrVA. The original values of L_z and L_x (shown Fig. 14 (b)) were measured as 35.950 mm and 26.880 mm. The length of the PZT stack was reduced by 20 μm to 35.980 mm by grinding the passive layer using wet & dry sandpaper. Then the PZT stack and the mechanical transformer were assembled with an 'interference fit' (Fig. 14 (c)) — the mechanical transformer was stretched along the z-axis and the PZT stack was pushed in. Measurements showed that the L_x and L_z were increased by 277 and 35 μm by the interference fit. Following that, the pre-stressing caps and bolts were applied, as shown in Fig. 14 (d). The nuts were tightened gradually by a torque wrench. When a torque of 0.4 Nm was applied, the mechanical transformer was compressed by the pre-stressing bolts to its original shape, indicated by L_x returning to 26.880 mm. In other words, the PSEH was pre-stressed to deform by 35 μm along the z-axis. Given the linear relationship between ΔL_z and the static pre-stress in the PZT stack presented in Fig. 11 (b), the static pre-stress is estimated to be ~32 MPa. Following that, the proof mass and the plate springs were installed, as shown in Figure (e).

4.2. Experimental setup

The PSEH was installed on an electromagnetic shaker (APS 113), as shown in Fig. 15. The acceleration generated by the shaker was measured by an accelerometer (8762A5, Kistler). A laser Doppler vibrometer (LDV) (OFV 534, Polytech) was used to measure the displacement of the proof mass. The PSEH was connected to a variable load resistor. The voltage across the load resistor was measured to calculate the average power output. For each actuating frequency, the load resistance was varied until the maximum power was recorded.

4.3. Lab test results and discussion

The measured and simulated performances of the PSEH actuated at 0.05 g are compared in Fig. 16. For simulation, the FEM with plate springs was used. Q_M was set to 140 so that the simulated power peak matched the measured. The simulated voltage $V$and optimal load resistance R_{opt}were converted to the corresponding values of the multilayer stack for comparison with experimental results by Eq. (3).

$$R^m_{opt} = \frac{R^s_{opt}}{N^2} V^m = \frac{V^s}{N} \tag{3}$$

where the subscripts m and s denote the values of N-layer and single-layer piezoelectric stack, respectively.

In the experiment, the PSEH produced two power peaks with a resonance bandwidthΔf = 6 Hz: 2.1 mW at 153.5 Hz and 2.5 mW at 159.5 Hz. The double power peaks validate the strong coupling of the PSEH. The simulation results show good agreement with the measured results in terms of power output, voltage output, optimal load resistance and displacement. However, it must be noted the effects of the softening nonlinearity of piezoelectric ceramics on the experimental results, as demonstrated in Fig. 16 (b). In the experiment, the internal impedance $|Z_{in}|$ was measured by a frequency response analyser (PSM1700, Newton 4th) at low excitation signals (0.2 V) and therefore with little nonlinear effects in the piezoelectric material. The measured$|Z_{in}|$ suggests that the resonance frequency of the PSEH is higher than the simulation. When actuated at 0.05 g, the elevated stress/strain in the piezoelectric material exhibits softening nonlinearity, leading to the reduction in the resonance frequency [47]. Because the optimal load resistance $R_{opt}$of a PEH is the internal impedance magnitude $|Z_{in}|$, the measured R_{opt} is $|Z_{in}|$ of PSEH with nonlinear behaviours of the piezoelectric material. R_{opt} and $|Z_{in}|$ has the minimum value around 153.5 Hz and the maximum value at 159.5 Hz. As a result, the voltage output at 159.5 Hz (2.75 V) is much higher than that at 153.5 Hz (0.25 V) as shown in Fig. 16 (c), although the power outputs at these two frequencies are about the same. The displacement in Fig. 16 (d) has two similar peaks corresponding to the two power peaks and two stress peaks of the mechanical transformer (Fig. 13 (a)).

The measured and simulated power outputs of the PSEH at different acceleration amplitude are presented in Fig. 17. As the acceleration amplitude is increased from 0.05 to 0.5 g, the first power peak frequency f_{01} decreases from 153.5 Hz to 151 Hz and the second power peak frequency f_{02} decreases from 159.5 to 157 Hz. The shift of the resonance frequency is a result of the softening nonlinearity of the piezoelectric material. As the acceleration is increased from 0.05 g to 0.5 g, the

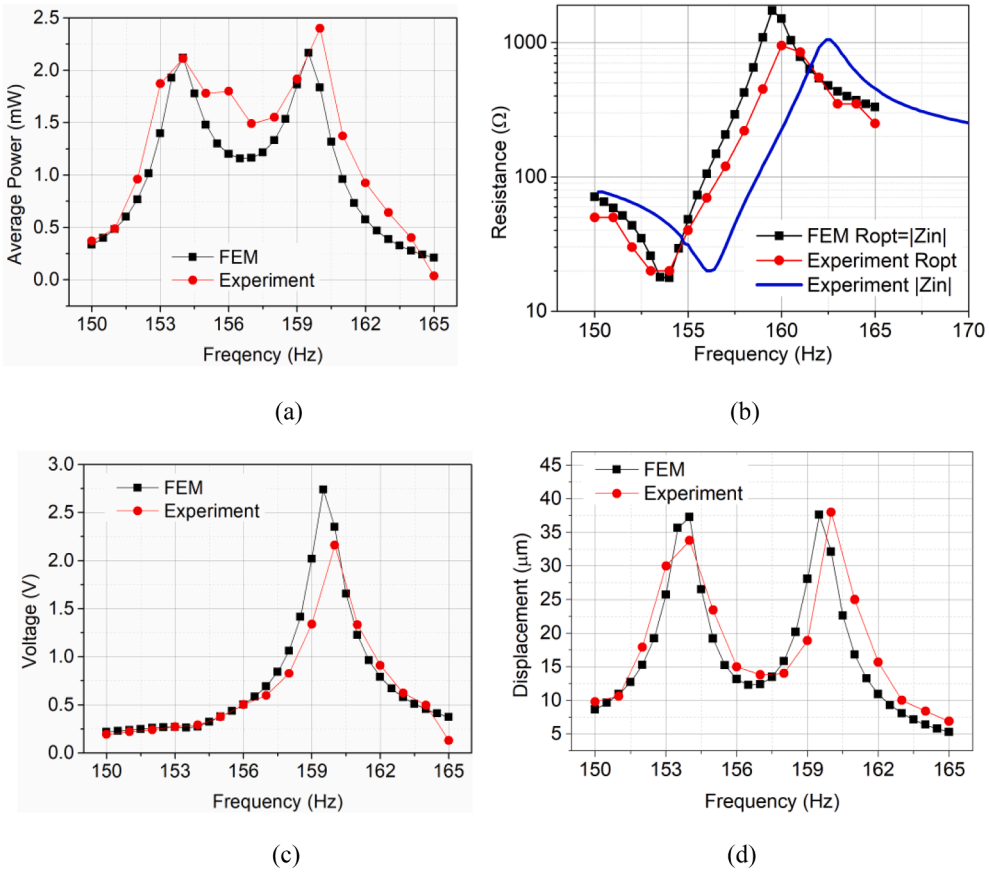

Fig. 16. Measured and simulated performances of the PSEH actuated at 0.05 g: (a) average power output, (b) optimal load resistance (c) the voltage amplitude across the optimal load resistance and (d) displacement amplitude of the proof mass.

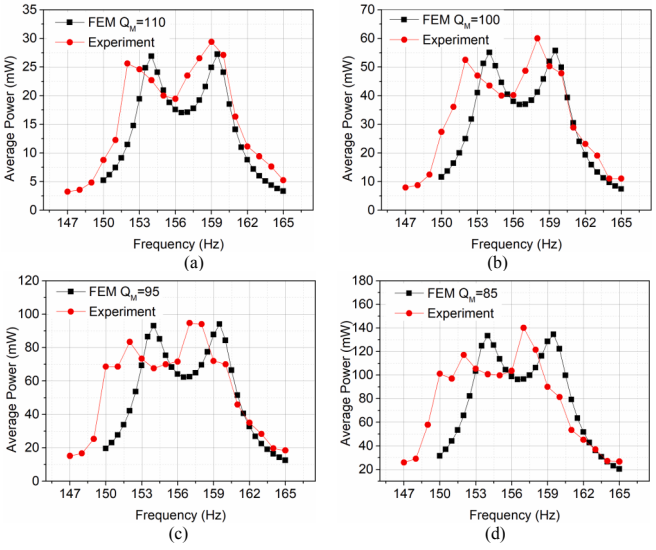

Fig. 17. Measured and simulated electric power outputs of the PSEH actuated at an acceleration of (a) 0.2 g, (b) 0.3 g, (c) 0.4 g and (d) 0.5 g.

mechanical quality factor Q_M in the FEM has to reduce from 140 to 85 so that the simulated power peaks match the experiment. The reduction in the mechanical quality factor Q_M implies the increase in the mechanical loss in the piezoelectric material, which is another consequence of the softening nonlinearity of piezoelectricity [48,49].

Table 2 summarises the measured performance of the PSEH. As the

Table 2
A summary of the measured performance of the PSEH at different accelerations.

Acceleration (g)	f_{01} (Hz)	f_{02} (Hz)	K^2	Q_M	K^2Q_M
0.2	152	159	0.094	110	10.4
0.3	152	158	0.081	100	8.1
0.4	152	157	0.067	95	6.4
0.5	152	157	0.067	85	5.7

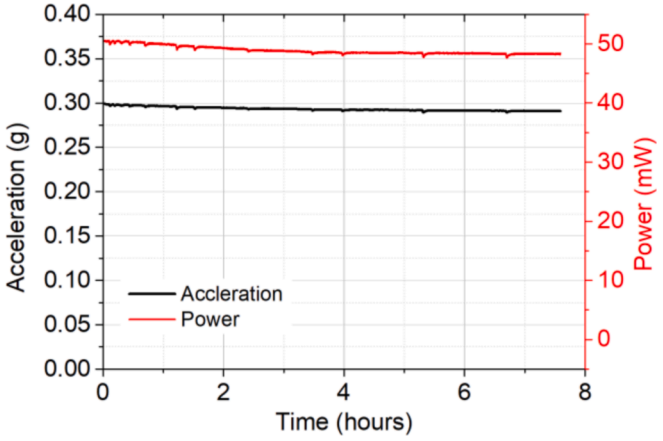

Fig. 18. Performance of the PSEH in a 7.9-hour continuous test.

Table 3
Performance comparison of the PSEH with the state-of-the-art inertial PEHs producing power.

References	Volume of PZT (mm^3)	Frequency (Hz)	Acceleration (g)	Power (mW)	Power density ($mW/cm^3/g^2$)
X. Li [50]	3140	87	0.5	14.6	18.6
Kim [14]	35 × 37 × 0.16 × 4	120	1	28	33.8
L. Wang [29]	7 × 7 × 32.4 × 3	37	0.1	26.42	554.7
Z. Yang [28]	32 × 15 × 0.7	25.7	0.5	54.7	651.2
This work	7 × 7 × 36	157	0.5	140	317.5

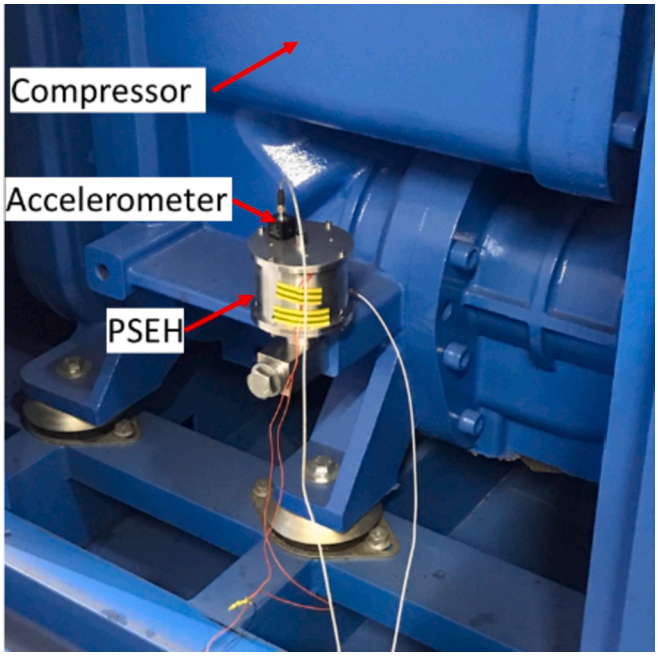

Fig. 19. PSEH installed on the compressor for on-site tests.

acceleration increases from 0.2 to 0.5 g, the value of K^2Q_M decreases from 10.4 to 5.7 due to the reduced electromechanically coupling coefficient K and mechanical quality factor Q_M. Nevertheless, the K^2Q_M is always much higher than 2, i.e. the PSEH is always strongly coupled, which can be validated by the two power peaks measured in the experiments. When actuated at 0.5 g, the PSEH produced 120 and 140 mW at 152 and 157 Hz, respectively. Moreover, the frequency range over which the power output is>1 mW is from 121 to 193 Hz, generating a 1-mW-bandwidth of as high as 72 Hz; the frequency range over which the power output is >10 mW is from 145 to 169 Hz, generating a 10-mW-bandwidth of 24 Hz.

To demonstrate the durability of the PSEH, the PSEH was actuated continuously for 7.9 h at 0.3 g, 157 Hz. The actuating acceleration and electric power output are shown in Fig. 18. The PSEH showed a quite stable power output at around 48 mW. The slight decrease in power is due to the decrease in the actuating acceleration. The stable relationship between the power output and the acceleration suggests the PSEH experienced no performance degradation.

The performance of the PSEH is compared with the state-of-the-art inertial PEHs in Table 3. The power density is defined as $\frac{power}{PZTvolume \times acceleration^2}$ [28]. The PSEH generates the highest power of 140 mW, which is 2.5 times the power reported in [28]. The power density of the PSEH is not the highest because the fatigue strength instead of the higher yield strength was used as the stress limit and a safety factor of 2 was applied. The safety margin compromised power output and power density. Nevertheless, power density can only be indicative when comparing different EHs because it does not reflect the actual power output or whether the EH can be scaled up to achieve high power.

5. On-site tests

5.1. Experimental methods

The PSEH was installed on the G-drive screw compressor, as shown in Fig. 19. A bespoke rig was designed to install the PSEH to the M20 threads on the compressor. An accelerometer (8762A5, Kistler) was used to measure input to the PSEH. The PSEH was connected to a variable load resistor. The voltage across the load resistor was measured to calculate the power generation. The testing was performed with the PSEH installed in two locations. The installation and the testing did not cause any interruption to the screw compressor, which worked as usual during the whole process.

5.2. On-site test results and discussions

The FFT of the accelerations measured on the compressor are presented in Fig. 20. The accelerations show frequency components at 157 and 315 Hz, which are nearly the same as the measurements that had been taken 9 months before this on-site test and presented previously in Fig. 1. Despite the high acceleration amplitude at 315 Hz, the voltage is mainly produced at 157 Hz, as shown in Fig. 20. At location 1, the PSEH produced a voltage of 2.33 V at 157 Hz compared to 0.083 V at 315 Hz; at location 2, the PSEH produced 5.80 V at 157 Hz, compared to 0.37 V at 315 Hz. Therefore, the acceleration at 157 Hz is responsible for most

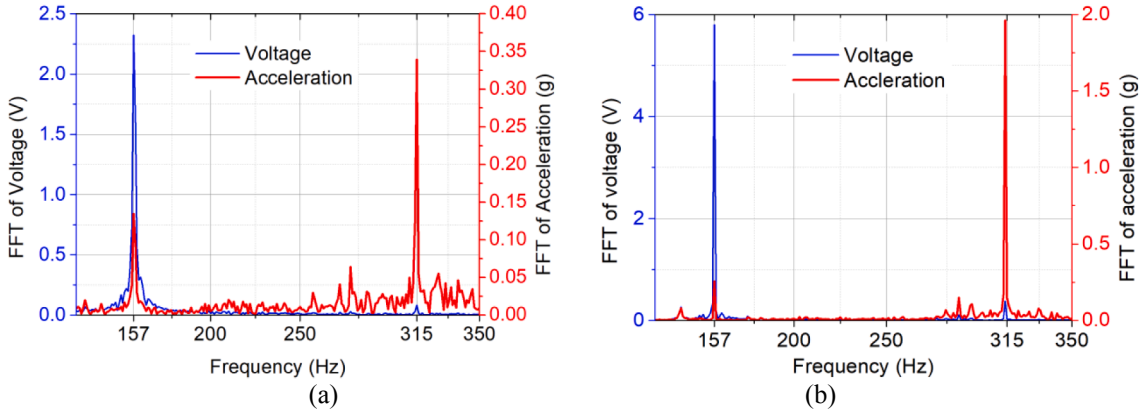

Fig. 20. Voltage and acceleration measured on PSEH connected to a 350 Ω load resistor at (a) Location 1 and (b) Location 2.

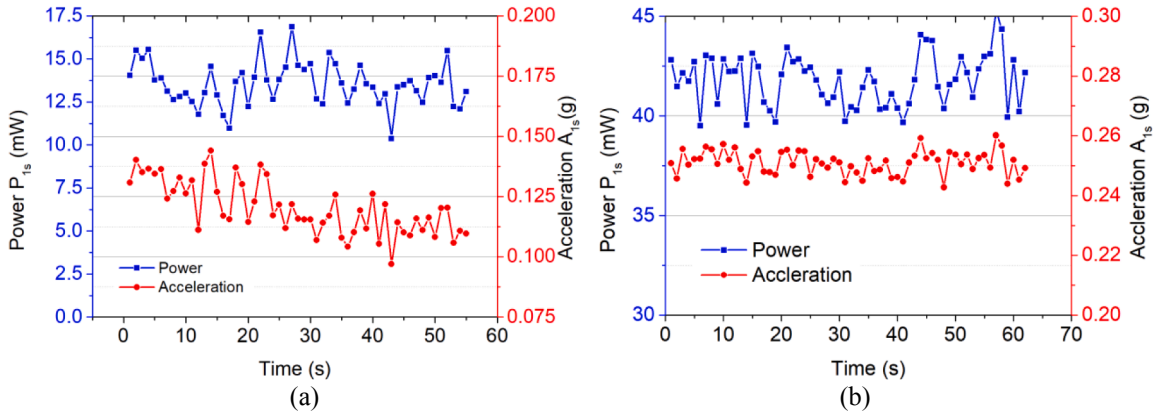

Fig. 21. Variation of the acceleration A_{1s} and power P_{1s} with time at (a) location 1 and (b) location 2.

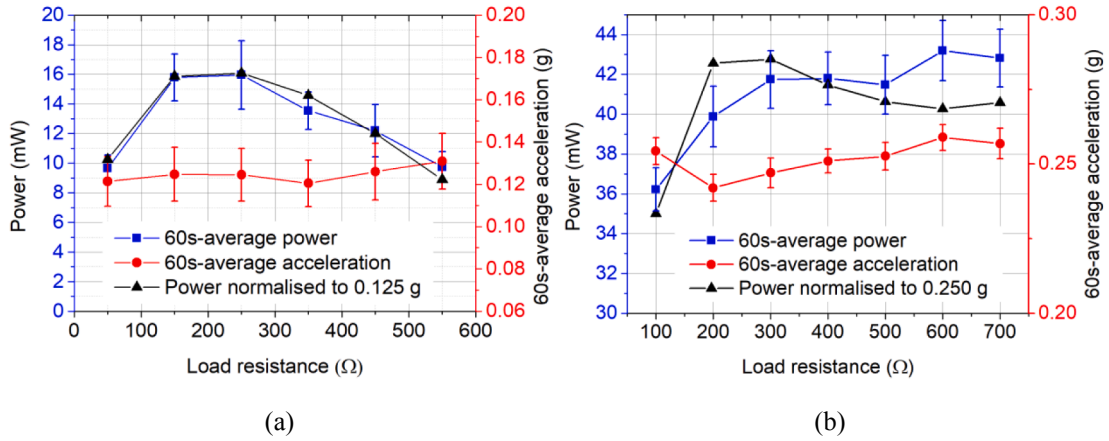

Fig. 22. Electrical power output and the input acceleration when the PSEH is connected to different load resistance (a) at Location 1 and (b) at Location 2.

of the power generation and the contribution of the acceleration at 314 Hz is negligible.

The vibration produced by the compressor fluctuated with time. Therefore, FFT was performed on the acceleration data of every one second period during a continuous test of 60 s. The amplitude of the 157-Hz component in every one second denoted as A_{1s}, is presented against time in Fig. 21. The mean value and standard division of A_{1s} are 0.121 g and 0.011 g, respectively at Location 1; they are 0.251 g and 0.004 g, respectively at Location 2. The power output averaged across every one second, denoted as P_{1s} follows the pattern of A_{1s}, as shown in Fig. 21. The mean value and standard division of P_{1s} are 13.54 mW and 1.26 mW, respectively at Location 1; they are 41.80 mW and 1.32 mW, respectively at Location 2.

A_{1s} and P_{1s} were averaged across 60 s to derive the 60 s-average power and the 60 s-average acceleration. Fig. 22 shows the 60 s-average power and 60 s-average acceleration against the load resistance connected to the PSEH. At Location 1, the maximum 60 s-average power recorded is 15.95 ± 2.30 mW when then PSEH is connected to a 250 Ω resistor and actuated at 0.125 ± 0.012 g. At Location 2, a maximum power of 43.19 ± 1.52 mW was observed when the PSEH was connected to a 600 Ω resistor and actuated at 0.259 ± 0.004 g. For different load resistance, the actuating acceleration from the compressor is slightly different. To identify the optimal load resistance, the 60 s-average powers at Location 1 and 2 were normalised to 0.125 g and 0.250 g, respectively based on the assumption that the power is linearly proportional to the square of acceleration. The normalised power indicates that the optimal load resistance of the PSEH is 250 Ω for both locations. This is expected as the optimal load resistance of the PSEH is mainly affected by the frequency.

6. Conclusions

In this paper, a durable and robust piezoelectric stack energy harvester (PSEH) with extremely high-power output has been developed for self-powered machine monitoring. The design of the PSEH incorporated systematic considerations not just on the power output but also on the durability and robustness for real-world applications. A piezoelectric-circuit coupled finite element model was developed to aid the design and was experimentally validated. The PSEH was tested both in the lab and on an industrial site.

The PZT stack in the PSEH experienced little stress concentration as it worked in a longitudinal mode. Its durability was increased by applying a compressive pre-stress to avoid the development of tensile stress since piezoelectric ceramics have a low tensile strength but high compressive strength. The axillary rig used to apply the pre-stress reduced the electromechanical coupling coefficient K and the resonance bandwidth of the PSEH. It had little effect on the power output because the use of the auxiliary rig resulted in a heavier proof mass to maintain the resonance frequency. By keeping the maximum stress in the mechanical transformer below half of the fatigue limit, the durability of the PSEH was increased. The robustness of the PSEH was strengthened by plate springs to minimise the effects of vibrations in undesired directions as the vibrations in real-world applications are usually multiple directional. These measures are effective in increasing the durability and robustness of the PSEH. The PSEH achieved strong coupling, demonstrated by the two power peaks in the resonance region and the value

of$K^2Q_M > 2$ with Q_M being the mechanical quality factor. When the actuating acceleration was increased in experiments, the piezoelectric material showed softening nonlinearity, which exhibited as a reduction in the electromechanical coupling coefficient K, mechanical quality factor Q_M and the resonance frequency. The PSEH maintained strong coupling despite the reduction of K and Q_M with the actuating acceleration.

With a factor of safety of 2, the PSEH showed a maximum power of 140 mW when actuated at 0.5 g, 157 Hz. The high power output enables the PSEH to continuously supply high-power-consumption wireless sensors while the high durability and robustness enable the PSEH to work safety in hash industrial environments. The developed PSEH is therefore meet the requirements for real-world applications.

CRediT authorship contribution statement

Yang Kuang: Conceptualization, Methodology, Validation, Investigation, Formal analysis, Writing - review & editing. **Zheng Jun Chew:** Investigation. **John Dunville:** Resources. **Jim Sibson:** Resources. **Meiling Zhu:** Supervision, Project administration, Funding acquisition, Writing - review & editing.

Declaration of Competing Interest

The authors declare that they have no known competing financial interests or personal relationships that could have appeared to influence the work reported in this paper.

Acknowledgement

The authors would like to acknowledge the support of the Engineering and Physical Science Research Council (EPSRC) through the grant 'Zero power, large area rail track monitoring' (EP/S024840/1) and the Royal Society through the Industrial Fellowship 'High Performance Energy Harvesting Sensor Systems for Critical Asset Monitoring' (INF/R2/202021).

References

[1] Tang X, Wang X, Cattley R, Gu F, Ball AD. Energy harvesting technologies for achieving self-powered wireless sensor networks in machine condition monitoring: A review. Sensors 2018;18(12):4113.
[2] Kande M, Isaksson AJ, Thottappillil R, Taylor N. Rotating electrical machine condition monitoring automation—A review. Machines 2017;5(4):24.
[3] Abdelkareem MA, et al. Vibration energy harvesting in automotive suspension system: A detailed review. Appl Energy 2018;229:672–99.
[4] Zhang J, Qin L. A tunable frequency up-conversion wideband piezoelectric vibration energy harvester for low-frequency variable environment using a novel impact-and rope-driven hybrid mechanism. Appl Energy 2019;240:26–34.
[5] Kuang Y, Hide R, Zhu M. Broadband energy harvesting by nonlinear magnetic rolling pendulum with subharmonic resonance. Appl Energy 2019/12/01/ 2019.; 255:113822.
[6] Fu H, Theodossiades S, Gunn B, Abdallah I, Chatzi E. Ultra-low frequency energy harvesting using bi-stability and rotary-translational motion in a magnet-tethered oscillator. Nonlinear Dyn 2020;101(4):2131–43.
[7] Guo X, Zhang Y, Fan K, Lee C, Wang F. A comprehensive study of non-linear air damping and "pull-in" effects on the electrostatic energy harvesters. Energy Convers Manage 2020;203:112264.
[8] Fan F-R, Tian Z-Q, Lin Wang Z. Flexible triboelectric generator. Nano Energy 2012; 1(2):328–34.
[9] Liu H, Zhong J, Lee C, Lee S-W, Lin L. A comprehensive review on piezoelectric energy harvesting technology: Materials, mechanisms, and applications. Appl Phys Rev 2018;5(4):041306.
[10] Yang Z, Zhou S, Zu J, Inman D. High-performance piezoelectric energy harvesters and their applications. Joule 2018;2(4):642–97.
[11] Qian F, Hajj MR, Zuo L. Bio-inspired bi-stable piezoelectric harvester for broadband vibration energy harvesting. Energy Convers Manage 2020;222: 113174.
[12] Hajati A, Kim S-G. Ultra-wide bandwidth piezoelectric energy harvesting. Appl Phys Lett 2011;99(8):083105.
[13] He L, Wang Z, Wu X, Zhang Z, Zhao D, Tian X. Analysis and experiment of magnetic excitation cantilever-type piezoelectric energy harvesters for rotational motion. Smart Mater Struct 2020;29(5):055043.
[14] Kim T, Ko Y, Yoo C, Choi B, Han S, Kim N. Design optimisation of wide-band piezoelectric energy harvesters for self-powered devices. Energy Convers Manage 2020;225:113443.
[15] Jeon DH, et al. A lever-type piezoelectric energy harvester with deformation-guiding mechanism for electric vehicle charging station on smart road. Energy 218: 119540.
[16] Upadrashta D, Yang Y, Tang L. Material strength consideration in the design optimization of nonlinear energy harvester. J Intell Mater Syst Struct 2014: 1045389X14546651.
[17] Anton S, Erturk A, Inman D. Strength analysis of piezoceramic materials for structural considerations in energy harvesting for UAVs. In: SPIE Smart Structures and Materials+ Nondestructive Evaluation and Health Monitoring, International Society for Optics and Photonics; 2010. p. 76430E-76430E-11.
[18] Okayasu M, Ozeki G, Mizuno M. Fatigue failure characteristics of lead zirconate titanate piezoelectric ceramics. J Eur Ceram Soc 2010;30(3):713–25.
[19] Kim HW, et al. Energy harvesting using a piezoelectric "cymbal" transducer in dynamic environment. Jpn J Appl Phys 2004;43(9A):6178–83.
[20] Qian F, Xu T-B, Zuo L. Design, optimization, modeling and testing of a piezoelectric footwear energy harvester. Energy Convers Manage 2018;171:1352–64.
[21] Qian F, Xu T-B, Zuo L. Piezoelectric energy harvesting from human walking using a two-stage amplification mechanism. Energy 2019;189:116140.
[22] Moure A, et al. Feasible integration in asphalt of piezoelectric cymbals for vibration energy harvesting. Energy Convers Manage 2016;112:246–53.
[23] Chen C, Sharafi A, Sun J-Q. A high density piezoelectric energy harvesting device from highway traffic–Design analysis and laboratory validation. Appl Energy 2020; 269:115073.
[24] Sharpes N, Vučković D, Priya S. Floor tile energy harvester for self-powered wireless occupancy sensing. Energy Harvest Syst 2016;3(1):43–60.
[25] Cao D-X, Duan X-J, Guo X-Y, Lai S-K. Design and performance enhancement of a force-amplified piezoelectric stack energy harvester under pressure fluctuations in hydraulic pipeline systems. Sens Actuators, A 2020;309:112031.
[26] Xu C, et al. Cantilever driving low frequency piezoelectric energy harvester using single crystal material 0.71 Pb (Mg1/3Nb2/3) O3–0.29 PbTiO3. Appl Phys Lett 2012;101(3):033502.
[27] Yang Z, Zu J. High-efficiency compressive-mode energy harvester enhanced by a multi-stage force amplification mechanism. Energy Convers Manage 2014;88: 829–33.
[28] Yang Z, Zhu Y, Zu J. Theoretical and experimental investigation of a nonlinear compressive-mode energy harvester with high power output under weak excitations. Smart Mater Struct 2015;24(2):025028.
[29] Wang L, Chen S, Zhou W, Xu T-B, Zuo L. Piezoelectric vibration energy harvester with two-stage force amplification. J Intell Mater Syst Struct 2017;28(9):1175–87.
[30] Zhao H, Ling J, Yu J. A comparative analysis of piezoelectric transducers for harvesting energy from asphalt pavement. J Ceram Soc Jpn 2012;120(1404): 317–23.
[31] Lei A, Xu R, Borregaard LM, Guizzetti M, Hansen O, Thomsen EV. Impedance based characterization of a high-coupled screen printed PZT thick film unimorph energy harvester. J Microelectromech Syst 2014;23(4):842–54.
[32] Siddiqui NA, Kim D-J, Overfelt RA, Prorok BC. Electromechanical coupling effects in tapered piezoelectric bimorphs for vibration energy harvesting. Microsyst Technol 2017;23(5):1537–51.
[33] Gibus D, et al. Strongly coupled piezoelectric cantilevers for broadband vibration energy harvesting. Appl Energy 2020;277:115518.
[34] Kuang Y, Chew ZJ, Zhu M. Strongly coupled piezoelectric energy harvesters: Finite element modelling and experimental validation. Energy Convers Manage 2020; 213:112855.
[35] Roundy S, Wright PK, Rabaey J. A study of low level vibrations as a power source for wireless sensor nodes. Comput Commun 2003;26(11):1131–44.
[36] Williams CB, Yates RB. Analysis of a micro-electric generator for microsystems. Sens Actuators A: Phys 1996;52(1-3):8–11.
[37] Yang K, Alice D, Meiling Z. A sandwiched piezoelectric transducer with flex end-caps for energy harvesting in large force environments. J Phys D Appl Phys 2017; 50(34):345501.
[38] Evans M, Tang L, Aw KC. Modelling and optimisation of a force amplification energy harvester. J Intell Mater Syst Struct 2018:1045389X18754352.
[39] Claeyssen F, Letty RL, Barillot F, Sosnicki O. Amplified piezoelectric actuators: Static & dynamic applications. Ferroelectrics 2007;351(1):3–14.
[40] Sherrit S, et al. Piezoelectric multilayer actuator life test. IEEE Trans Ultrason Ferroelectr Freq Control 2011;58(4):820–8.
[41] Pertsch P, Richter S, Kopsch D, Krämer N, Pogodzik J, Hennig E. Reliability of piezoelectric multilayer actuators. In: Proceed. Conf. ACTUATOR.-Germany, Bremen; 2006. p. 1-3.
[42] Chen W, Wang Y, Deng W. Deformable force amplification frame promoting piezoelectric stack energy harvesting: Parametric model, experiments and energy analysis. J Intell Mater Syst Struct 2017;28(7):827–36.
[43] Kong N, Ha DS, Erturk A, Inman DJ. Resistive Impedance Matching Circuit for Piezoelectric Energy Harvesting. (in English), J Intell Mater Syst Struct Article; Proceedings Paper 2010;21(13):1293-1302.
[44] Zhao H, Hui W, Nie Y, Weng Y, Dong H. Very high cycle fatigue fracture behavior of high strength spring steel 60Si2CrVA. Chin J Mater Res 2008;22:526–32.
[45] Grigg S, et al. Development of a low-power wireless acoustic emission sensor node for aerospace applications. Struct Control Health Monit e2701.
[46] Ashby MF, Jones DRH. Engineering materials 1: an introduction to properties, applications and design. Elsevier; 2012.
[47] Leadenham S, Moura A, Erturk A. Exploiting material softening in hard PZTs for resonant bandwidth enhancement. In: Active and Passive Smart Structures and

Integrated Systems 2016, vol. 9799. International Society for Optics and Photonics; 2016. 97992F.

[48] Leadenham S, Erturk A. Modeling and characterization of elastic, coupling, and dissipative nonlinearities in PZT bimorphs for vibration energy harvesting. In: ASME 2014 Dynamic Systems and Control Conference. American Society of Mechanical Engineers Digital Collection; 2014.

[49] Kuang Y, Sadiq M, Cochran S, Huang Z. High-power characterization of a microcutter actuated by PMN-PT piezocrystals. IEEE Trans Ultrason Ferroelectr Freq Control 2015;62(11):1957–67.

[50] Li X, Guo M, Dong S. A flex-compressive-mode piezoelectric transducer for mechanical vibration/strain energy harvesting. IEEE Trans Ultrason Ferroelectr Frequency Control 2011;58(4):698–703.